van der Waals Epitaxial Growth of Graphene on Sapphire by Chemical Vapor Deposition without a Metal Catalyst

Jeonghyun Hwang,[†,||,]* Moonkyung Kim,[†,||] Dorr Campbell,[†] Hussain A. Alsalman,[†] Joon Young Kwak,[†] Shriram Shivaraman,[†] Arthur R. Woll,[‡] Arunima K. Singh,[§] Richard G. Hennig,[§] Sandeep Gorantla,[⊥] Mark H. Rümmeli,[⊥] and Michael G. Spencer[†]

[†]School of Electrical and Computer Engineering, [‡]Cornell High Energy Synchrotron Source (CHESS), and [§]Department of Materials Science & Engineering, Cornell University, Ithaca, New York 14853, United States and [⊥]Leibniz-Institute for Solid State and Materials Research, IFW Dresden, 01069 Dresden, Germany. [||]These authors contributed equally to this work.

ABSTRACT van der Waals epitaxial growth of graphene on c-plane (0001) sapphire by CVD without a metal catalyst is presented. The effects of CH_4 partial pressure, growth temperature, and H_2/CH_4 ratio were investigated and growth conditions optimized. The formation of monolayer graphene was shown by Raman spectroscopy, optical transmission, grazing incidence X-ray diffraction (GIXRD), and low voltage transmission electron microscopy (LVTEM). Electrical analysis revealed that a room temperature Hall mobility above 2000 $cm^2/V \cdot s$ was achieved, and the mobility and carrier type were

correlated to growth conditions. Both GIXRD and LVTEM studies confirm a dominant crystal orientation (principally graphene [10−10] || sapphire [11−20]) for about 80−90% of the material concomitant with epitaxial growth. The initial phase of the nucleation and the lateral growth from the nucleation seeds were observed using atomic force microscopy. The initial nuclei density was ∼24 μm^{-2}, and a lateral growth rate of ∼82 nm/min was determined. Density functional theory calculations reveal that the binding between graphene and sapphire is dominated by weak dispersion interactions and indicate that the epitaxial relation as observed by GIXRD is due to preferential binding of small molecules on sapphire during early stages of graphene formation.
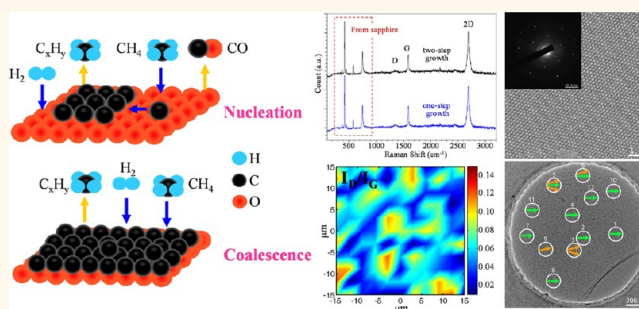
KEYWORDS: graphene · sapphire · CVD · van der Waals · epitaxy · Raman

Graphene is a one atom thick honeycomb-shaped 2D sheet of sp^2-bonded carbon atoms with extraordinary material properties such as extremely high carrier mobility, high optical transparency, and high surface area/mass ratio.[1−5] Graphene is also a member of sp^2-bonded 2D monolayer materials, which include boron nitride (BN)[6,7] and molybdenum disulfide (MoS_2).[8] Heterojunctions (both vertical and lateral) of graphene and other 2D materials are opening up exciting new device and materials possibilities.

In order to realize the whole potential of 2D materials, it is essential to develop a practical growth technique and understand the nature of growth. Catalyst-free growth of graphene on an insulating substrate can eliminate problematic transfer processes and has been studied on several different substrates. Polycrystalline graphitic film was grown on sapphire[9] and (111) Si[10] by molecular beam epitaxy (MBE). Graphene syntheses on MgO,[11] SiO_2,[12,13] Si_3N_4,[14] HfO_2,[14] BN,[15,16] and sapphire[17] were studied using low-temperature (∼400 °C) or conventional (950−1000 °C) CVD. However, these methods have not produced material to date competitive with either graphene grown on metal such as Ni and Cu[18,19] or epitaxial graphene on SiC.[3,20] Typically, defect-related Raman D-peak is larger than G-mode in these samples, indicating small grain size (≤14 nm)[21,22] and carrier mobility is limited to 1,[9] 40,[12] or 100−600 $cm^2/V \cdot s$.[17] Oxygen-aided synthesis on SiO_2,[23] remote catalyzation on silica,[24] and CVD on Cu/dielectrics and in situ evaporation of Cu[25] were also reported. With these techniques, the Raman D-peak significantly decreased, but the carrier mobility did not improve much (531 $cm^2/V \cdot s$ in ref 23 and 100−600 $cm^2/V \cdot s$ in ref 24). High-temperature

CVD (1550−1650 °C) route produced well-ordered graphitic film[26] or graphene[27] on sapphire with material qualities as close as those of graphene on metal or SiC. This material exhibited the Raman I_D/I_G value of 0.05 with ∼3000 $cm^2/V \cdot s$ Hall mobility, suitable for practical applications.[27] However, the growth optimization was not fully explored in that study other than growth temperature, and the growth mechanism was not well examined regarding nucleation and epitaxial relation.

Here, we report graphene growth on c-plane (0001) sapphire, which can be viewed as van der Waals epitaxy. We also present a growth model and growth mechanism by carefully investigating the initial stages of growth, the epitaxial relationship of the graphene to the sapphire, and the binding energy between the film and substrate. The van der Waals epitaxy[28−30] of 2D materials involves the epitaxial growth of a layered material that proceeds with a van der Waals force resulting in good epitaxy even with large lattice mismatch between the grown and substrate material. It was observed that the substrate and film grown with van der Waals epitaxy are rotationally commensurate, in spite of the fact that their lattice constants are usually incommensurate with each other. The van der Waals epitaxial growth mechanism differs significantly from the sublimation growth of graphene produced by the thermal decomposition of SiC under ultrahigh vacuum (UHV)[3] or atmospheric argon pressure[20] at high temperatures. In the sublimation approach, graphene is aligned to the substrate due to step flow evaporation of Si. Growth of graphene on sapphire examined in this study also differs from CVD of graphene on single- and polycrystalline transition metals.[18,19] While van der Waals epitaxy is the likely growth mechanism for CVD on metals, the strong catalytic action of the metals allows for the cracking of the methane at much lower temperatures than those used in this study.

RESULTS AND DISCUSSION

Graphene growth using methane (CH_4) required a high partial pressure of methane. For example, if methane concentration is lower than ∼0.2%, graphene or graphitic films were not formed at a growth temperature higher than 1450 °C regardless of growth time and the amount of hydrogen flowed. We believe that the suppression of graphene growth is due to carbon etching by hydrogen[31] and oxygen[32] (carbothermal reduction of sapphire), which is more dominant at high temperatures with the low CH_4 partial pressures. Hydrogen, which we supply during the growth, is the first source of carbon etching through the formation of hydrocarbon gases. Sapphire (Al_2O_3) is stable at high temperature but starts to decompose at much lower temperature, if it comes into contact with carbon, by releasing CO. This "carbo-thermal reduction of sapphire"[32] is another very important

carbon etching process in this growth. A two-step growth was employed in the case of the low methane concentration (<∼0.2%) to promote the nucleation at a lower temperature (≤1350 °C), and lateral expansion of the nuclei was performed at a higher temperature (where nucleation of graphene is suppressed). The effect of methane partial pressure on nucleation was examined using the two-step growth at a temperature between 950 and 1450 °C with a fixed methane concentration of 0.15% and the H_2/CH_4 ratio of 10. After the nucleation, graphene was grown at 1550 °C with the same methane flow and H_2/CH_4 ratio. The detailed data can be seen in the Supporting Information. If the nucleation temperature is higher than ∼1350 °C, no growth was observed with the given methane partial pressure. As the CH_4 concentration decreased from 0.15 to 0.08%, the critical nucleation temperature also dropped from 1350 to 1225 °C, independent of nucleation time. This is the same observation that the one-step direct growth is not possible at a temperature higher than ∼1450 °C when the methane partial pressure is lower than 0.2%. From this study, it was found that the critical nucleation temperature increases as the methane partial pressure increases.

A small amount of hydrogen was added during the growth in order to promote the decomposition of methane and 2D growth.[31] It was observed that the surface of graphene became rough and started to form 3D island-like structures when the H_2/CH_4 ratio was smaller than the optimum point. If the ratio is too high, no graphene was produced. This behavior was still observed even with a prolonged nucleation or growth time. The highest possible H_2/CH_4 ratio was desirable to obtain the higher quality graphene as long as the condition allowed the formation of graphene. However, the optimum range of the ratio was narrow, and the final result varied widely, showing growth or no growth of graphene. Also, the effect of nucleation and growth temperature was investigated. As expected from the previous results,[26,27] the higher the nucleation/growth temperature is, the higher the crystal quality of grown graphene is. It is inferred that higher growth temperatures enhance the surface mobility of active carbon and produces higher quality crystals. The detailed data of the H_2/CH_4 ratio and growth temperature can be found in the Supporting Information.

Growth times were adjusted to obtain a monolayer graphene with a full coverage ranging from 45 s to 5 min depending on other growth conditions. It was observed that higher growth temperature or lower H_2/CH_4 ratio needed less growth time once the methane partial pressure is higher than the critical value and allows the growth of graphene. It indicates that the methane cracking efficiency increases more rapidly than the carbon etching rate by hydrogen or oxygen as growth temperature increases.
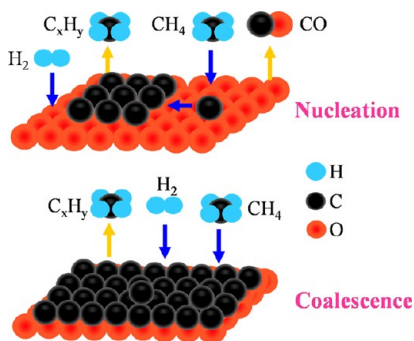
Figure 1. Growth model for CVD graphene on sapphire. Carbon is supplied by the cracking of CH₄, and it is balanced by carbon etching by hydrogen and oxygen. Aluminum atoms on the sapphire surface were not shown here for a simplified view.

All of these observations suggest a growth model, as shown in a simplified drawing of Figure 1, balancing carbon supply and carbon removals. Carbon is supplied by the thermal cracking of methane, and carbon is removed by the hydrogen etching forming hydrocarbon gases and the carbo-thermal reduction process releasing carbon monoxide (CO). Once the sapphire surface is completely covered by the first layer of graphene, the sapphire surface is protected and one of the carbon removal processes (etching by oxygen originated from the sapphire substrate) would stop working. In this case, it is expected that the growth rate increases. To support this, we did additional experiments by heating graphene on sapphire under Ar environment (600 Torr). Two types of graphene samples were prepared. The first one was exfoliated graphene (5 and 20 μm) obtained by mechanical cleaving of kish graphite, and they were transferred on sapphire. The other sample was prepared like the atomic force microscopy (AFM) image in Figure 3c (small grain graphene patches on sapphire by incomplete CVD growth on sapphire). Then, the samples were annealed at a growth temperature (1550−1650 °C) without methane and hydrogen flow. After the annealing, small graphene patches of the second sample all disappeared, leaving an etching mark and roughening of the sapphire surface. However, the large graphene sheet from the exfoliation stayed on the sapphire surface without any noticeable change in the surface roughness. This experiment supports that the large area graphene patch or sheet can protect the sapphire surface at high growth temperature, resulting in less carbon etching by oxygen. This also agrees quite well with our experimental observations showing a super linear increase of graphene thickness after one layer growth. This makes it difficult to control the thickness of multilayer graphene. The detailed mechanism of nucleation and growth of the second layer is not well understood at this point, and future investigation is needed. With an optimized condition, both the high-temperature direct growth and the two-step
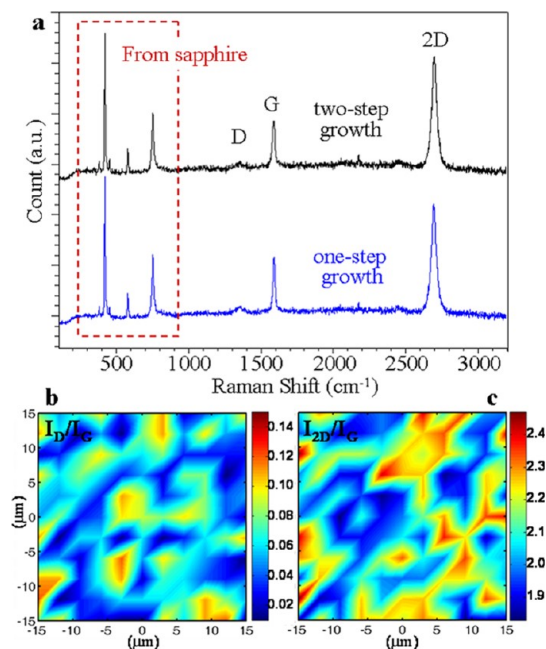

Figure 2. Raman spectroscopy analysis of graphene on sapphire. (a) (Bottom) Raman spectrum of graphene grown directly at 1550 °C with CH₄ concentration of 1.2% and H₂/CH₄ ratio of 12. (Top) Raman spectrum of graphene nucleated at 1350 °C for 3 min with a H₂/CH₄ flow ratio of 14 and then grown at a temperature of 1650 °C with a H₂/CH₄ flow ratio of 10. The partial pressure of CH₄ was 0.15% for both the nucleation and high-temperature growth. (b,c) Raman mapping of one-step growth sample over 30 μm × 30 μm area. (b) I_D/I_G and (c) I_{2D}/I_G.

growth produced a monolayer graphene on sapphire, as confirmed by Raman spectroscopy, optical transmission measurement, grazing incidence X-ray diffraction (GIXRD), and low voltage transmission electron microscopy (LVTEM).

Figure 2 shows Raman spectroscopy data of graphene grown on sapphire by the high-temperature direct growth and the two-step method after all optimization. For the direct growth, samples were grown at 1550 °C with a CH₄ concentration of 1.2% and a H₂/CH₄ ratio of 12. In the cases of the two-step method, the samples were nucleated at 1350 °C for 3 min with a H₂/CH₄ flow ratio of 14 and then grown at a temperature between 1450 and 1650 °C with a H₂/CH₄ flow ratio of 10. The partial pressure of CH₄ was 0.15% for both the nucleation and high-temperature growth. These were the optimum growth conditions determined by Raman, AFM, and electrical measurements. The detailed optimization process can be found in the Supporting Information. The Raman spectra in Figure 2a shows the signature of graphene with the G-peak (∼1580 cm⁻¹) associated with the in-plane vibration and the 2D-peak (∼2700 cm⁻¹) from a second-order process involving two phonons. In most of the samples, the Raman I_{2D}/I_G ratios are about 2, which can be interpreted as a thin film (1−2 ML).[18,33−36] Also, the curve fitting of the 2D-peaks showed that they are single Lorentzian with the
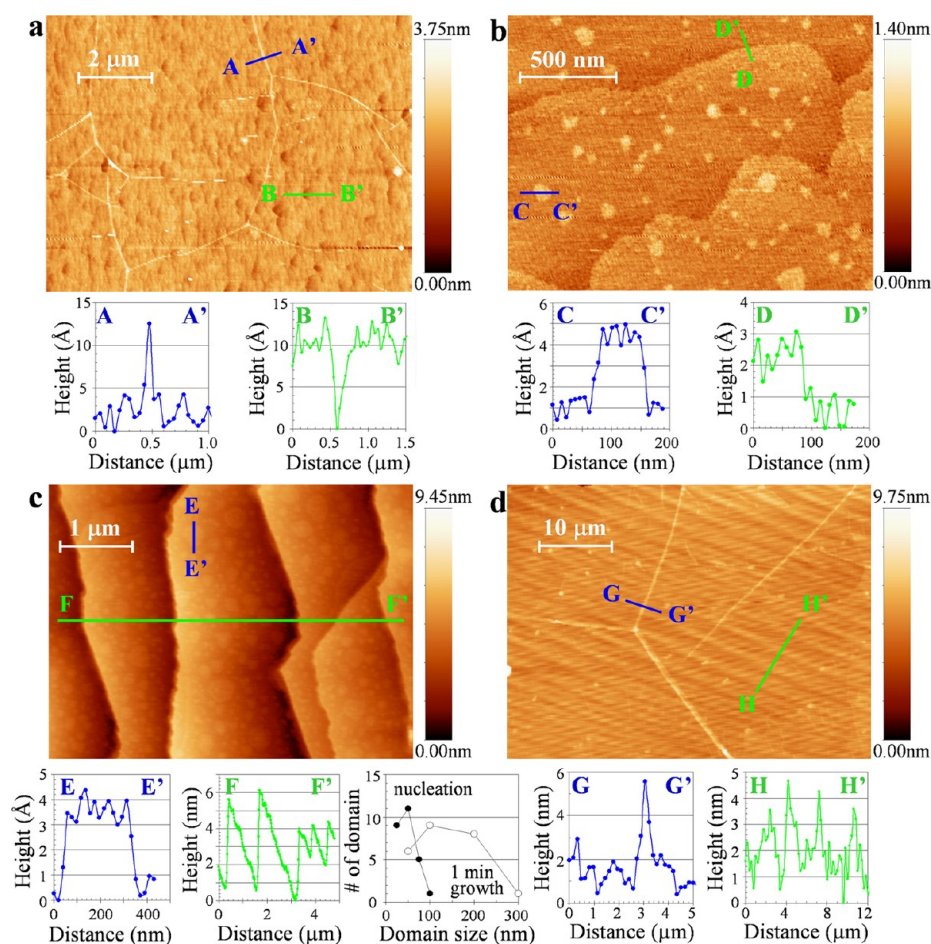
Figure 3. AFM analysis of graphene on sapphire. (a) Graphene was directly grown at 1550 °C for 3 min with CH$_4$ concentration of 0.8% and a H$_2$/CH$_4$ ratio of 12. **(b)** AFM of "nucleation only" sample. This sample was nucleated at 1350 °C for 3 min with the CH$_4$ concentration of 0.15% and a H$_2$/CH$_4$ ratio of 14 and then immediately cooled. **(c)** AFM of "partially grown" sample. This sample was nucleated at the same condition described in panel b and then grown at 1650 °C for 1 min with a CH$_4$ concentration of 0.15% and a H$_2$/CH$_4$ ratio of 10. It was an intentional incomplete growth to see the lateral growth of nucleation domains. The size distributions of the graphene domains in a 1 μm^2 area are shown here together. Solid circles indicate the distribution after nucleation as seen in panel b, and the open circles represent the distribution after nucleation +1 min short growth as seen in panel c. **(d)** This sample was grown by the two-step method. This sample was nucleated and then grown at the same condition of panels b and c but for 3 min at 1650 °C to complete growth.

best fwhm values of 43 and 33 cm^{-1} for the sample directly grown at 1550 °C and the sample nucleated at 1350 °C and grown at 1650 °C, respectively, indicating a high-quality monolayer graphene.[34−37] Disorder-induced D-peaks (~1350 cm^{-1}) were also detected with the ratio of the D-peak to G-peak intensity (I_D/I_G) varying depending on growth conditions. The Raman I_D/I_G ratio has been known to be inversely proportional to crystallite or grain size and was extensively used in this study to estimate the quality of graphene and the degree of disorder.[21,22] The grain size of this material can be estimated to be ~270 nm, based on the formula[22] L_a(nm) = 2.4 × 10^{-10} × λ^4 × (I_D/I_G)$^{-1}$, when the wavelength of the excitation laser, λ, is 488 nm and the I_D/I_G ratio is 0.05. Figure 2b,c shows Raman mapping of a one-step growth sample (I_D/I_G and I_{2D}/I_G over 30 μm × 30 μm area). The excitation laser spot is about 1.5 μm, and Raman data were obtained at every 1.5 μm. These maps show the uniformity of this material, and

the average values of I_D/I_G and I_{2D}/I_G are 0.06 and 2.1, respectively, in this area. There was no noticeable difference in the uniformity of two-step growth sample, as measured by the same Raman mapping, and the average values of I_D/I_G and I_{2D}/I_G were 0.05 and 2.2 over the same 30 μm × 30 μm area.

Figure 3 shows AFM images and height profiles of graphene on sapphire. Graphene grown by the high-temperature direct method is seen in Figure 3a. This sample was grown at 1550 °C for 3 min with a CH$_4$ concentration of 0.8% and a H$_2$/CH$_4$ ratio of 12. Several white lines were observed, and the heights are measured to be approximately 12 Å as seen in the profile AA′. These folds are seen in many large area graphene films such as epitaxial graphene or CVD graphene on metal. Some roughening of the sapphire surface was also observed with pit formation, the depth of which is about 10 Å as shown in profile BB′. This could be caused by the carbo-thermal reduction process of the sapphire

surface. The root-mean-square (rms) roughness over a 2.0 μm $\times$ 2.0 μm area, where there is no fold, was 1.9−2.4 Å. Another direct growth sample with 1.2% CH_4 showed almost the same surface features, but the rms roughness varied between 2.8 and 3.7 Å on the same size areas.

The early stage of graphene growth was studied with a low CH_4 concentration since the growth rate during the high-temperature direct growth with a high methane flow is too high to control precisely. Figure 3b shows an AFM image of "nucleation only" sample. It was nucleated at 1350 °C for 3 min with a CH_4 concentration of 0.15% and a H_2/CH_4 ratio of 14. The growth stopped and cooled immediately after the nucleation step without completing the actual high-temperature growth. Many white speck-like features sized between 25 and 100 nm are seen in Figure 3b, and it is believed that those spots are nucleation sites. The height measurements across the spots, shown in profile CC′ revealed that they were about 3−4 Å high, which agreed well with the thickness of 1 ML graphene.[18,34,38] The nucleation density was roughly estimated to be $\sim$26 μm^{-2} by counting the white features. The horizontal wavy lines are thought to be steps of (0001) sapphire, and the height of the steps is about 2.2 Å as seen in profile DD′. This matches with the reported value of a sapphire unit step ($c/6$, where c = 12.99 Å is the vertical direction lattice constant of c-plane sapphire) before annealing.[39] The rms roughness over this 2.0 μm $\times$ 2.0 μm area was 1.2 Å. Nucleation domains were uniformly distributed across the sample surface with no discernible tendency for step edge nucleation.

Figure 3c shows an AFM image of a sample nucleated at 1350 °C like the sample in Figure 3b and then grown at 1650 °C for 1 min with a CH_4 concentration of 0.15% and a H_2/CH_4 ratio of 10. It was intentionally grown for a shorter time (1 min) at the high temperature to see the growth of nucleation domains. The circular-shaped white features were also observed, and sizes ranged from about 50 to 350 nm. The height of these features was about 3−4 Å (profile EE′)[18,34,38] like the one in Figure 3b profile CC′, but the lateral size increased as compared to the ones in Figure 3b. The step heights of sapphire (profile FF′) increased significantly due to step bunching under high temperature.[39] The density of domains was estimated to be $\sim$24 μm^{-2} and shown to be almost the same as that of the nucleation stage in Figure 3b. The size distribution of the domains in a 1 μm^2 area is seen together with the distribution after nucleation. The solid and open circles represent the distribution of "after nucleation" and "after 1 min growth", respectively. Most seeds in Figure 3b have domain sizes between 25 and 50 nm with an average value of 48 nm after nucleation. However, the distribution became broader and shifted to the right side (larger size) after nucleation +1 min

short growth. The average grain diameter was 130 nm. If we can assume that the average-sized nucleation seed grew and became one of the average-sized grains in Figure 3c, then the lateral growth rate would be $\sim$82 nm/min. The rms roughness over this 5.0 μm $\times$ 5.0 μm area was 12.1 Å, but it dropped to 1.5 Å if we only considered a 0.5 μm $\times$ 3.0 μm area on the terrace of sapphire. After completing a full growth cycle (3 min nucleation and 3 min high-temperature growth), the surface feature associated with graphene was not very distinguishable by AFM in a small scan area and only the sapphire steps were observed. However, if a larger area was scanned, the folds of graphene similar to the ones seen in Figure 3a were observed. They are shown in the profile GG′ of Figure 3d along with the sapphire surface morphology (profile HH′).

High-resolution X-ray photoelectron spectroscopy (XPS) measurements (see Figure S4 in the Supporting Information) showed that there are no detectable chemical bonds of Al−C (281.5 eV)[40] or Al−O−C (282.5 eV)[40] at the graphene/sapphire interface, indicating that the grown graphene is suspended on the sapphire substrate. This result also agrees with the previous report by Fanton et al.[27] and our density functional theory (DFT) calculation described in this paper. However, the folds observed by AFM suggest a compressive strain in the grown graphene. Compressive strains could be built in the graphene during the cool down process due to the mismatch of thermal expansion coefficient, and probably the strains were partially relieved by the formation of folds or wrinkles. However, we did not observe any obvious relation between the wrinkles and surface features of the sapphire substrate in either one-step growth (Figure 3a) or two-step growth (Figure 3d). Some wrinkles or folds start at the step edge or etch pits of sapphire, but some of them do not.

Strain in the grown graphene was also investigated by tracing the Raman 2D-peak position. Raman 2D-peaks are slightly blue-shifted in these graphene on sapphire compared to exfoliated monolayer graphene,[36] and the positions range from $\sim$2697 cm^{-1} (growth at 1450 °C) to $\sim$2704 cm^{-1} (1650 °C) when the graphene samples were grown by the one-step method with a methane partial pressure larger than 0.6% (see Figure 4 and the section for electrical properties). The 2D-peak position almost linearly increased as the growth temperature increased from 1450 to 1650 °C ($\sim$1.8 cm^{-1} per 50 °C), and these shifts in the 2D-peak correspond to compressive strains smaller than $\sim$0.3%.[41] The blue shift of 2D-peak can be caused by hole doping[42] or compressive strain,[41,43] but the main reason in these samples is attributed to the compressive strains since Hall effect measurements showed that these graphene are n-type and the charge densities are very small. It is known that the 2D-peak width linearly increases as a function of strain, so approximately 3 cm^{-1} broader
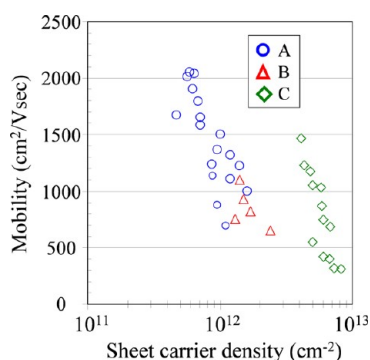
Figure 4. Electrical properties of graphene on sapphire determined by Hall effect measurements. Graphene samples represented by group A (CH_4 concentration >0.6%) and group B (0.2% < CH_4 concentration $\leq$ 0.6%) were directly grown at 1550 °C. Samples in group C were grown with the two-step method at a temperature between 1600 and 1650 °C with a CH_4 concentration lower than 0.2%. Samples in group A are n-type, and the others in groups B and C are p-type.
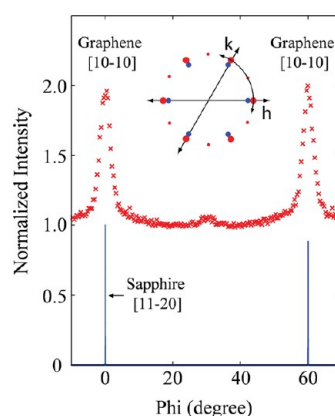

Figure 5. Epitaxial relation between grown graphene and sapphire substrate determined by GIXRD. XRD azimuthal scans by rotating the sample about the surface normal, through graphene {10−10} and sapphire {11−20} peaks. Graphene [10−10] is mainly aligned to sapphire [11−20].

2D-peak is expected with the maximum strain value of 0.3%.[43] A recent report also showed that 2D-peak intensity can be varied due to strains, but a consistent trend or a quantitative relation was not presented in that study.[44] This effect needs to be accounted for in Raman analysis (such as I_{2D}/I_G), but more future research is required to be able make a conclusive statement. In other growths (one-step growth with a lower methane partial pressure or two-step growth), Raman also showed a slight blue shift of 2D-peak. In these cases, the grown graphene are p-type (see Figure 4), suggesting that the upshift is due to the combined effects of compressive strain and hole doping.

Room temperature ambient Hall measurements on 6 mm × 6 mm size samples showed that the mobility of grown graphene was 300−2050 $cm^2/V \cdot s$ with a sheet carrier density of 5 × 10^{11} to 8 × 10^{12} cm^{-2}. Note that this includes non-optimized samples to see a trend of mobility and carrier density. The relation between mobility and carrier density can be categorized into three groups, as shown in Figure 4. The relatively higher mobility with a lower carrier density shown in group A was obtained when the samples were grown at a high temperature (1550 °C) directly with a CH_4 concentration higher than ∼0.6%. Under this growth condition, all of the grown graphene were n-type. However, if samples were grown with a CH_4 concentration lower than ∼0.6%, all of the grown graphene turned out to be p-type. They are seen in groups B and C. Samples in group B were obtained using a direct growth method with a methane concentration lower than ∼0.6% but higher than ∼0.2%. Graphene grown with a two-step method with an even lower methane partial pressure (≤0.2%) is shown in group C. Samples in group C have relatively higher sheet carrier densities between 4 × 10^{12} and 8 × 10^{12} cm^{-2}, compared to other samples directly grown at high temperature. The

origin of this different carrier type is not well understood at this time, but it is speculated that oxygen is doped in the p-type samples. The p-type samples were grown when the CH_4 concentration was relatively lower, so oxygen at the sapphire surface can be incorporated into the growth through site competition against the cracked down methane molecules. The positions of G- and 2D-peaks were carefully investigated to see the doping effect. In the case of group A, the G- and 2D-peaks were found approximately at 1586 and 2700 cm^{-1}, respectively. However, those moved to ∼1587 and ∼2704 cm^{-1} in group B and to ∼1589 and ∼2707 cm^{-1} in group C at the sample growth temperature. These blue shifts of G- and 2D-peaks could be attributed to hole doping rather than compressive strain since the ratios in the blue shifts of G- and 2D-peaks do not agree well with a known value (1:3).[42,45] High-resolution XPS spectra (C1s and O1s) were also obtained from the p-type sample to examine the oxygen incorporation. As shown in the Figure S4 (see Supporting Information), there were no distinct split peaks associated with carbon−oxygen bonds, but the combined percentage of carbon−oxygen bonds in the C1s and O1s peaks is not trivial and this would explain the p-type conductivity in the sample. Inside each group, no strong trend was observed between the CH_4 partial pressure and mobility or between the Raman I_D/I_G and mobility once the samples were grown with an optimized condition. In many cases, the carrier mobility data were not presented in the metal-free growth of graphene on insulating or dielectric substrates. The best Hall mobility of ∼2000 $cm^2/V \cdot s$ with ∼7 × 10^{12} cm^{-2} sheet carrier density in this study is higher than that of most other metal-free growths[9−17,23−25] and comparable to the previous result[27] of high-temperature CVD on sapphire (as grown sample before vacuum annealing treatment).

Epitaxial relation of the grown graphene was determined using grazing incidence X-ray diffraction. Figure 5

shows azimuthal scans, corresponding to rotation of the sample about the surface normal, through the graphene {10−10} and sapphire {11−20} peaks. The scans show that the grown graphene has 60° rotational symmetry, and the graphene unit cells are principally rotated by 30° with respect to those of sapphire. This result contrasts with those reported earlier,[26] which exhibited graphitic domains whose [10−10] directions were aligned, in equal proportion, to both the sapphire [11−20] and sapphire [10−10]. Here, there is a small amount (~5%) of intensity at $\varphi = 30°$, corresponding to graphene [10−10] ‖ sapphire [10−10]. The film in Figure 5 was grown at the optimal conditions as determined by Raman measurements described above. Films grown at other conditions were found to be very similar to that in Figure 5, but growth at nonideal conditions showed a larger proportion of misaligned graphene grains aligned with [10−10] ‖ sapphire [10−10]. In addition to azimuthal scans as in Figure 5, out-of-plane XRD scans along the graphene [10−1L] direction, such as those (in Figure 4 and ref 26), were also performed. As expected for monolayer graphene, and in contrast to the previous results,[26] these scans (shown in Figure S5 of Supporting Information) exhibit a slow, monotonic decay of intensity from grazing incidence through Q_perp = 1 graphite reciprocal lattice units (rlu). On the basis of prior studies,[26] we interpret the absence of intensity modulation through this region to indicate the absence of multiple graphene layers.

To further investigate the grain alignment, we employed low voltage transmission electron microscopy to evaluate the fabricated graphene sheets after transfer. A typical example of a transferred sheet residing on a holey carbon Quantifoil TEM grid is provided on Figure 6a. Observations of the graphene material (Figure 6b,c) indicate that the material is for the most part monolayer. See, for example, the small hole at the bottom of Figure 6c, which confirms monolayer graphene. To investigate the crystalline order of the material, selected area electron diffraction (SAED) was conducted at various positions on graphene sheets several times for each sample. Figure 6b shows the different positions investigated by SAED from a graphene sheet fabricated using a one-step process (see Figure S7 in the Supporting Information for an equivalent example from a graphene sheet grown through a two-step route). From the SAED pattern, we evaluate the relative orientation of the graphene at the different spatial positions investigated. Most SAED patterns show only six reflex spots that arise due to graphene's six-fold symmetry and correspond to a signal from a single domain (Figure 6d). Other SAED patterns show more than six spots (Figure 6e), which indicate multiple domains. More detailed studies using dark-field imaging, on such an area having multiple sets of reflex, enable one to confirm and map multiple grains. Figure 6f shows an example in false colors (note this is

not from the 12 investigation points shown in Figure 6b). This multiple domain region is intentionally shown here since it is difficult to see the polycrystalline nature at a location having a large single grain. The individual dark-field images of the grains are provided in Figure S8. By comparing all of the SAED patterns, one can determine the relative crystal orientations for different locations along a graphene sheet, and this can be easily represented using arrows placed within the circles where the SAED was collected as shown in Figure 6b and Figures S6 and S7 in Supporting Information. It is obvious from these arrows that a single dominant orientation exists. However, sometimes there are deviations from the dominant direction. We investigated numerous sheets for single-step and two-step grown graphene samples with at least 12 SAED measurements in each case. The relative angles between them can be found in Tables S1 and S2 and frequency plots for Figures S6 and S7 in the Supporting Information. In all cases, we observe that approximately 80% of the graphene area has a preferential crystal orientation within a ±3° range (in the frequency plots for Figures S6 and S7, the central area within ±3° range below the Lorentzian fits is about 80% of the total area). This finding is concomitant with that of the GIXRD studies; namely, a dominant graphene orientation exists in the as-produced graphene.

In order to elucidate the origin of the epitaxial relation between sapphire and graphene, we calculate the binding energy of graphene on sapphire and of a small graphene fragment on sapphire for different orientations. For the binding of graphene to sapphire, we systematically determine all possible epitaxial relationships by constructing supercells for graphene on the Al-terminated (0001) surface of sapphire. Allowing the graphene to be strained by up to 3% and searching over cells with lattice vectors up to 23 Å ensures that we identify all possible alignments with small induced strains and short repeat length that may be energetically favorable. The method of finding these commensurate cells is described in detail in the Supporting Information.

For the three smallest commensurate cells, we calculate the binding energy of graphene to the Al-terminated (0001) surface of sapphire using density functional theory (DFT). The binding energy calculations are performed with two exchange-correlation functionals, the generalized gradient approximation PBE[46−49] and the vdW-DF which is a nonlocal correlation functional added to the revPBE functional to account for dispersion interactions.[50,51] Figure 7 shows the resulting epitaxial relationships and binding energies. The PBE functional, which lacks a description of the dispersion interaction, does not result in any significant binding energy, indicating a lack of electrostatic or bonding interactions between the sapphire surface and graphene. In contrast, the vdW-DF functional
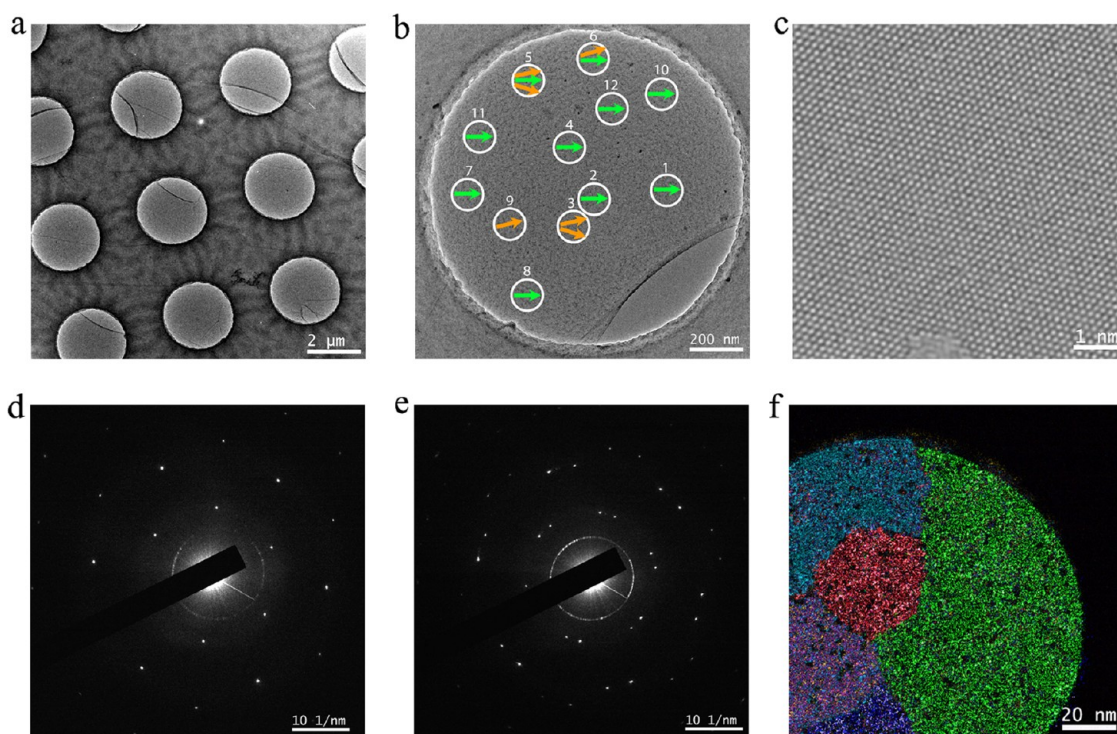
Figure 6. LVTEM evaluations of the produced graphene confirming a dominant crystal orientation. (a) Overview of LVTEM micrograph of a transferred graphene sheet (single-step growth). (b) Magnified region showing graphene residing over a single hole on the grid. The different locations from which SAED patterns were acquired are indicated by white circles. The orientation of the graphene grains in these locations normalized with respect to orientation of the SAED pattern taken from region 1 is represented by arrows. Green arrows represent the dominant crystal orientation, while orange arrows indicate a deviation of greater the 3° from the dominant orientation. (c) LVTEM image of monolayer graphene (note the small hole at the bottom of the image confirming monolayer graphene). (d,e) Two SAED patterns corresponding to (d) a single grain and (e) two grains. (f) False colored dark-field TEM image showing a region with multiple grains with different crystal orientations.
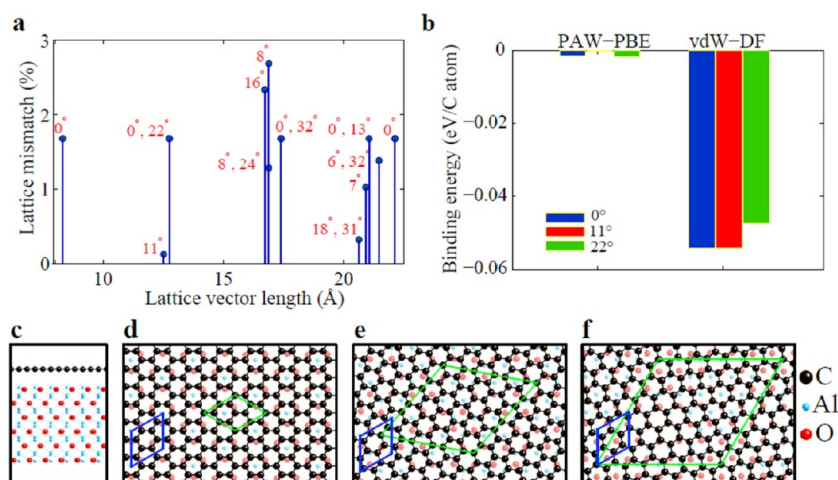

Figure 7. Theoretical calculation. (a) Lattice mismatch and orientation plotted with a lattice vector length of the commensurate cell. (b) Calculated binding energy of sapphire and graphene for three orientations with different functionals shows that dispersion interactions between sapphire and graphene dominate and that the binding is independent of orientation of graphene on sapphire. (c) Side view of a commensurate cell. (d−f) Three commensurate cells with orientations of (d) 0°, (e) 11°, and (f) 22° have lattice mismatches of 1.68, 0.13, and 1.68% respectively.

results in a binding energy of about 45 meV per carbon atom and a binding distance of 3.1 Å for all three cells, demonstrating that the interaction between graphene and sapphire is dominated by dispersion interactions. The similarity of the binding energy for all three commensurate cells shows that the dispersion interaction only weakly depends on the orientation of the graphene layer on the sapphire surface.

The strain on the graphene required to obtain a commensurate epitaxial relation between the graphene and sapphire significantly reduces the binding energy. Considering the observed variation in the

binding energy, which is significantly smaller than 20 meV per carbon atom, we find that strains larger than about 0.5% would reduce the binding energy so much as to make these configurations unfavorable. The two observations that (i) the binding energy is dominated by dispersion interactions that do not depend significantly on the orientation between graphene and sapphire and (ii) that any strain significantly reduces the binding energy indicate that the experimentally observed orientation relation between graphene and sapphire is not due to a preferential binding between graphene and sapphire.

To determine if the observed orientation relation could be a result of the nucleation, we calculate the binding energy of a small graphene fragment, pyrene, on the (0001) sapphire surface. The calculations show that the binding energy strongly depends on the rotation angle of the pyrene ranging from about 60 to over 100 meV per carbon atom. Altogether, the density functional calculations for graphene and pyrene on sapphire show that the experimentally observed preferential orientation of graphene on sapphire is most likely developed at the early stages of the graphene layer formation when nucleation occurs in the presence of small hydrocarbons such as methane, benzene, pyrene, *etc*. It is likely that a critical graphene fragment size exists above which the binding energy becomes independent of orientation and below which the small graphene fragments bind to sapphire preferentially and coalesce to form larger grain such as those present in the experimental samples.

CONCLUSIONS

We have proved that a high-quality monolayer graphene can be grown by van der Waals epitaxy on a *c*-plane sapphire substrate. Raman spectroscopy, optical transmission, GIXRD, and TEM showed the nature of monolayer graphene. The quality of graphene measured by the Raman I_D/I_G improved as the nucleation and growth temperature increased. Hydrogen played an important role in obtaining high-quality films. High hydrogen flow causes complete etching of surface carbon, but the best quality graphene was achieved with a hydrogen flow just slightly lower than this critical value. Room temperature Hall effect measurements showed that more than 2000 $cm^2/V \cdot s$ mobility can be obtained with an optimized growth and the grown graphene can have a different type of carrier depending on growth condition. The p-type samples were obtained when the methane partial pressure is lower than 0.6%, and n-type graphene was grown if the concentration is higher than the critical point. AFM showed that the nucleation was not initiated at a specific site, but the nucleation seeds were uniformly distributed on the sapphire surface. Also, the lateral two-dimensional growth of the domains was observed, and the growth rate was estimated. Epitaxial relation determined by GIXRD revealed that the grown graphene has 60° rotational symmetry and the unit cells of graphene are mainly rotated by 30° compared to those of sapphire substrate. The LVTEM studies show monolayer graphene which is partly polycrystalline; nonetheless, detailed spatial SAED studies confirm a single dominant crystal orientation for around 80% of the material. DFT calculations show that the binding between sapphire and graphene is dominated by dispersion interactions and only weakly depends on the orientation. The preferential binding orientation of small graphene fragments on sapphire during early stages of formation is likely the origin of the experimentally observed epitaxial orientation relation. The rotational alignment to the substrate and the theoretical calculations support the assertion that this growth can be described as van der Waals epitaxy. This van der Waals epitaxy could be applied to the growth and analysis of other 2D materials and their heterostructures, which have strong bonding only in the 2D direction but van der Waals nature at the interface.

METHODS

Growth. A conventional vertical cold wall CVD system, which was originally developed for SiC epitaxy, was used for this study. Graphite filaments located below the wafer carrier were heated by DC electric power, and growth temperature was monitored by pyrometers. The main carrier gas for the growth was argon (Ar) with a flow rate of ~10 000 sccm, and methane (CH_4) and hydrogen (H_2) were introduced independently. Methane was used as a carbon source with a flow rate between 5 and 200 sccm. The flow rate of hydrogen was 5–15 times more than that of methane, and the H_2/CH_4 flow ratio was varied to optimize the growth. Chamber pressure was kept at 600 Torr. Graphene was grown directly at a high temperature when the methane partial pressure was higher than 0.2%. Two-step growth was employed when the methane concentration was lower than 0.2%, which consisted of lower temperature nucleation at 1250–1350 °C for a short time (2–3 min) followed by an actual growth at higher temperature of 1450 to 1650 °C. The typical growth time for the higher temperature (1450 to 1650 °C) growth was 45 s to 5 min. Samples were cooled (at a rate of 150 °C/min) right after growth, under Ar but without methane or hydrogen flow.

Characterizations. Grown samples were characterized by Raman microscopy (Renishaw InVia) utilizing a 488 nm Ar ion laser and ambient atomic force microscopy (Veeco Dimension 3100). Carrier type, mobility, and sheet density were obtained by Hall effect measurements at room temperature with a magnetic field of 0.2 T. The grown samples were cleaved into 6 mm × 6 mm size, and metal contacts were made with indium (In) dots using a conventional van der Pauw contact geometry. Infrared transmission experiments were conducted in a Nicolet 8700 Research FT-IR spectrometer over the energy range of 0.25–0.85 eV using a KBr beam splitter and MCT detector. A motorized precision stage was employed to alternate between

the sample and reference. Successive scans were averaged to improve the signal-to-noise ratio. XPS measurements were carried out in an angle-resolved (with a takeoff angle of 20° for higher surface sensitivity) ultrahigh vacuum system (Surface Science SSX-100) using an Al Kα X-rays at 1486.66 eV. Curve fitting of the spectra was carried out using a Gaussian−Lorentzian peak shape after Shirley background correction. GIXRD data were obtained at the G2 station at Cornell High Energy Synchrotron Source (CHESS) using a beam energy of 10.0 ± 0.01 keV ($\lambda = 0.124$ nm), selected using a single-crystal Be crystal monochromator. Motorized slits were used to define a 0.2×2 ($V \times H$) mm^2 beam, with a typical flux of 5×10^{10} photons/s. Data were collected using a 640-element 1D diode array, each element of which incorporates its own pulse counting electronics and is capable of count rates of $\sim 10^5$ photons/s. For grazing incidence diffraction, a set of 0.1° Soller slits were used on the detector arm to define the in-plane resolution. The low voltage aberration-corrected transmission electron microscopy studies were conducted on a JEOL 2010F retrofitted with both image and probe spherical aberration (Cs) correctors by CEOS. All measurements were conducted using an acceleration voltage of 80 kV. Dark-field LVTEM was carried out using an objective aperture to filter the diffraction spots corresponding to individual graphene grains. Selected area electron diffraction patterns were acquired using the smallest SAED aperture allowing a viewing area of *ca.* 100 nm. The graphene was transferred to holey carbon Quantifoil TEM grids using a poly-(methyl methacrylate)-based transfer route. The detailed description of this graphene transfer from the sapphire substrate will be published in a forthcoming article.

DFT Calculation. All binding energies were calculated by means of DFT simulations using the Vienna Ab-initio Simulation Package (VASP).[52−55] The core states were described by the projector-augmented wave method. Calculations are performed with the PBE and vdW-DF revPBE exchange-correlation functionals. The 0, 11, and 22° orientations were represented by commensurate cells with 38, 264, and 446 atoms, respectively, as shown in Figure 7d−f. A cutoff energy of 700 eV and a vacuum separation between the periodic images of the slabs of 10 Å ensure convergence of the binding energy to better than 1 meV per carbon atom. The Brillouin zone integration was performed using k-point meshes with 20 points Å^{-1} and a Gaussian smearing with a width of 0.2 eV. Relaxations of the structures were performed until the forces were below 0.05 eV/Å. Cells with 236 atoms were used for computing the binding energies of pyrene on sapphire. For this cell size, interactions of pyrene with its periodic images were found to be below 4 meV per carbon atom.

Conflict of Interest: The authors declare no competing financial interest.

Supporting Information Available: Growth optimization using Raman I_D/I_G, I_{2D}/I_G, and 2D-peak width. XPS spectra (C1s and O1s) of p-type sample. Out-of-plane XRD data. LVTEM SAED spatial studies and dark-field images. Determination of commensurate lattice vectors of graphene on sapphire for DFT calculation. This material is available free of charge *via* the Internet at http://pubs.acs.org.

REFERENCES AND NOTES

1. Novoselov, K. S.; Geim, A. K.; Morozov, S. V.; Jiang, D.; Katsnelson, M. I.; Grigorieva, I. V.; Dubonos, S. V.; Firsov, A. A. Two-Dimensional Gas of Massless Dirac Fermions in Graphene. *Nature* **2005**, *438*, 197–200.

2. Zhang, Y.; Tan, Y. W.; Stormer, H. L.; Kim, P. Experimental Observation of the Quantum Hall Effect and Berry's Phase in Graphene. *Nature* **2005**, *438*, 201–204.

3. Berger, C.; Song, Z. M.; Li, T. B.; Li, X. B.; Ogbazghi, A. Y.; Feng, R.; Dai, Z. T.; Marchenkov, A. N.; Conrad, E. H.; First, P. N.; *et al.* Ultrathin Epitaxial Graphite: 2D Electron Gas Properties and a Route toward Graphene-Based Nanoelectronics. *J. Phys. Chem. B* **2004**, *108*, 19912–19916.

4. Bolotin, K. I.; Sikes, K. J.; Jiang, Z.; Klima, M.; Fudenberg, G.; Hone, J.; Kim, P.; Stormer, H. L. Ultrahigh Electron Mobility in Suspended Graphene. *Solid State Commun.* **2008**, *146*, 351–355.

5. Kim, K. S.; Zhao, Y.; Jang, H.; Lee, S. Y.; Kim, J. M.; Kim, K. S.; Ahn, J. H.; Kim, P.; Choi, J. Y.; Hong, B. H. Large-Scale Pattern Growth of Graphene Films for Stretchable Transparent Electrodes. *Nature* **2009**, *457*, 706–710.

6. Ci, L.; Song, L.; Jin, C. H.; Jariwala, D.; Wu, D. X.; Li, Y. J.; Srivastava, A.; Wang, Z. F.; Storr, K.; Balicas, L.; *et al.* Atomic Layers of Hybridized Boron Nitride and Graphene Domains. *Nat. Mater.* **2010**, *9*, 430–435.

7. Shi, Y. M.; Hamsen, C.; Jia, X. T.; Kim, K. K.; Reina, A.; Hofmann, M.; Hsu, A. L.; Zhang, K.; Li, H. N.; Juang, Z. Y.; *et al.* Synthesis of Few-Layer Hexagonal Boron Nitride Thin Film by Chemical Vapor Deposition. *Nano Lett.* **2010**, *10*, 4134–4139.

8. Radisavljevic, B.; Radenovic, A.; Brivio, J.; Giacometti, V.; Kis, A. Single-Layer MoS$_2$ Transistors. *Nat. Nanotechnol.* **2011**, *6*, 147–150.

9. Jerng, S. K.; Yu, D. S.; Kim, Y. S.; Ryou, J.; Hong, S.; Kim, C.; Yoon, S.; Efetov, D. K.; Kim, P.; Chun, S. H. Nanocrystalline Graphite Growth on Sapphire by Carbon Molecular Beam Epitaxy. *J. Phys. Chem. C* **2011**, *115*, 4491–4494.

10. Hackley, J.; Ali, D.; DiPasquale, J.; Demaree, J. D.; Richardson, C. J. K. Graphitic Carbon Growth on Si(111) Using Solid Source Molecular Beam Epitaxy. *Appl. Phys. Lett.* **2009**, *95*, 133114-1–133114-3.

11. Rummeli, M. H.; Bachmatiuk, A.; Scott, A.; Borrnert, F.; Warner, J. H.; Hoffman, V.; Lin, J. H.; Cuniberti, G.; Buchner, B. Direct Low-Temperature Nanographene CVD Synthesis over a Dielectric Insulator. *ACS Nano* **2010**, *4*, 4206–4210.

12. Sun, J.; Lindvall, N.; Cole, M. T.; Wang, T.; Booth, T. J.; Boggild, P.; Teo, K. B. K.; Liu, J.; Yurgens, A. Controllable Chemical Vapor Deposition of Large Area Uniform Nanocrystalline Graphene Directly on Silicon Dioxide. *J. Appl. Phys.* **2012**, *111*, 044103-1–044103-6.

13. Medina, H.; Lin, Y. C.; Jin, C. H.; Lu, C. C.; Yeh, C. H.; Huang, K. P.; Suenaga, K.; Robertson, J.; Chiu, P. W. Metal-Free Growth of Nanographene on Silicon Oxides for Transparent Conducting Applications. *Adv. Funct. Mater.* **2012**, *22*, 2123–2128.

14. Sun, J.; Lindvall, N.; Cole, M. T.; Teo, K. B. K.; Yurgens, A. Large-Area Uniform Graphene-like Thin Films Grown by Chemical Vapor Deposition Directly on Silicon Nitride. *Appl. Phys. Lett.* **2011**, *98*, 252107-1–252107-3.

15. Son, M.; Lim, H.; Hong, M.; Choi, H. C. Direct Growth of Graphene Pad on Exfoliated Hexagonal Boron Nitride Surface. *Nanoscale* **2011**, *3*, 3089–3093.

16. Ding, X. L.; Ding, G. Q.; Xie, X. M.; Huang, F. Q.; Jiang, M. H. Direct Growth of Few Layer Graphene on Hexagonal Boron Nitride by Chemical Vapor Deposition. *Carbon* **2011**, *49*, 2522–2525.

17. Song, H. J.; Son, M.; Park, C.; Lim, H.; Levendorf, M. P.; Tsen, A. W.; Park, J.; Choi, H. C. Large Scale Metal-Free Synthesis of Graphene on Sapphire and Transfer-Free Device Fabrication. *Nanoscale* **2012**, *4*, 3050–3054.

18. Reina, A.; Jia, X. T.; Ho, J.; Nezich, D.; Son, H. B.; Bulovic, V.; Dresselhaus, M. S.; Kong, J. Large Area, Few-Layer Graphene Films on Arbitrary Substrates by Chemical Vapor Deposition. *Nano Lett.* **2009**, *9*, 30–35.

19. Li, X. S.; Cai, W. W.; An, J. H.; Kim, S.; Nah, J.; Yang, D. X.; Piner, R.; Velamakanni, A.; Jung, I.; Tutuc, E.; *et al.* Large-Area Synthesis of High-Quality and Uniform Graphene Films on Copper Foils. *Science* **2009**, *324*, 1312–1314.

20. Emtsev, K. V.; Bostwick, A.; Horn, K.; Jobst, J.; Kellogg, G. L.; Ley, L.; McChesney, J. L.; Ohta, T.; Reshanov, S. A.; Rohrl, J.; et al. Towards Wafer-Size Graphene Layers by Atmospheric Pressure Graphitization of Silicon Carbide. *Nat. Mater.* **2009**, *8*, 203–207.

21. Tuinstra, F.; Koenig, J. L. Raman Spectrum of Graphite. *J. Chem. Phys.* **1970**, *53*, 1126–1130.

22. Cancado, L. G.; Takai, K.; Enoki, T.; Endo, M.; Kim, Y. A.; Mizusaki, H.; Jorio, A.; Coelho, L. N.; Magalhaes-Paniago, R.; Pimenta, M. A. General Equation for the Determination of the Crystallite Size L_a of Nanographite by Raman Spectroscopy. *Appl. Phys. Lett.* **2006**, *88*, 163106-1–163106-3.

23. Chen, J. Y.; Wen, Y. G.; Guo, Y. L.; Wu, B.; Huang, L. P.; Xue, Y. Z.; Geng, D. C.; Wang, D.; Yu, G.; Liu, Y. Q. Oxygen-Aided Synthesis of Polycrystalline Graphene on Silicon Dioxide Substrates. *J. Am. Chem. Soc.* **2011**, *133*, 17548–17551.

24. Teng, P. Y.; Lu, C. C.; Akiyama-Hasegawa, K.; Lin, Y. C.; Yeh, C. H.; Suenaga, K.; Chiu, P. W. Remote Catalyzation for Direct Formation of Graphene Layers on Oxides. *Nano Lett.* **2012**, *12*, 1379–1384.

25. Ismach, A.; Druzgalski, C.; Penwell, S.; Schwartzberg, A.; Zheng, M.; Javey, A.; Bokor, J.; Zhang, Y. G. Direct Chemical Vapor Deposition of Graphene on Dielectric Surfaces. *Nano Lett.* **2010**, *10*, 1542–1548.

26. Hwang, J.; Shields, V. B.; Thomas, C. I.; Shivaraman, S.; Hao, D.; Kim, M.; Woll, A. R.; Tompa, G. S.; Spencer, M. G. Epitaxial Growth of Graphitic Carbon on C-Face SiC and Sapphire by Chemical Vapor Deposition (CVD). *J. Cryst. Growth* **2010**, *312*, 3219–3224.

27. Fanton, M. A.; Robinson, J. A.; Puls, C.; Liu, Y.; Hollander, M. J.; Weiland, B. E.; LaBella, M.; Trumbull, K.; Kasarda, R.; Howsare, C.; et al. Characterization of Graphene Films and Transistors Grown on Sapphire by Metal-Free Chemical Vapor Deposition. *ACS Nano* **2011**, *5*, 8062–8069.

28. Koma, A. Van der Waals Epitaxy—A New Epitaxial Growth Method for a Highly Lattice Mismatched System. *Thin Solid Films* **1992**, *216*, 72–76.

29. Koma, A.; Ueno, K.; Saiki, K. Heteroepitaxial Growth by van der Waals Interaction in One-Dimensional, Two-Dimensional and Three-Dimensional Materials. *J. Cryst. Growth* **1991**, *111*, 1029–1032.

30. Ohuchi, F. S.; Shimada, T.; Parkinson, B. A.; Ueno, K.; Koma, A. Growth of $MoSe_2$ Thin Films with van der Waals Epitaxy. *J. Cryst. Growth* **1991**, *111*, 1033–1037.

31. Vlassiouk, I.; Regmi, M.; Fulvio, P. F.; Dai, S.; Datskos, P.; Eres, G.; Smirnov, S. Role of Hydrogen in Chemical Vapor Deposition Growth of Large Single-Crystal Graphene. *ACS Nano* **2011**, *5*, 6069–6076.

32. Cox, J. H.; Pidgeon, L. M. An Investigation of Aluminum-Oxygen-Carbon System. *Can. J. Chem.* **1963**, *41*, 671–683.

33. Lee, D. S.; Riedl, C.; Krauss, B.; von Klitzing, K.; Starke, U.; Smet, J. H. Raman Spectra of Epitaxial Graphene on SiC and of Epitaxial Graphene Transferred to SiO_2. *Nano Lett.* **2008**, *8*, 4320–4325.

34. Lee, S.; Lee, K.; Zhong, Z. H. Wafer Scale Homogeneous Bilayer Graphene Films by Chemical Vapor Deposition. *Nano Lett.* **2010**, *10*, 4702–4707.

35. Graf, D.; Molitor, F.; Ensslin, K.; Stampfer, C.; Jungen, A.; Hierold, C.; Wirtz, L. Spatially Resolved Raman Spectroscopy of Single- and Few-Layer Graphene. *Nano Lett.* **2007**, *7*, 238–242.

36. Malard, L. M.; Pimenta, M. A.; Dresselhaus, G.; Dresselhaus, M. S. Raman Spectroscopy in Graphene. *Phys. Rep.* **2009**, *473*, 51–87.

37. Ferrari, A. C.; Meyer, J. C.; Scardaci, V.; Casiraghi, C.; Lazzeri, M.; Mauri, F.; Piscanec, S.; Jiang, D.; Novoselov, K. S.; Roth, S.; et al. Raman Spectrum of Graphene and Graphene Layers. *Phys. Rev. Lett.* **2006**, *97*, 187401-1–187401-4.

38. Gupta, A.; Chen, G.; Joshi, P.; Tadigadapa, S.; Eklund, P. C. Raman Scattering from High-Frequency Phonons in Supported N-Graphene Layer Films. *Nano Lett.* **2006**, *6*, 2667–2673.

39. Cuccureddu, F.; Murphy, S.; Shvets, I. V.; Porcu, M.; Zandbergen, H. W.; Sidorov, N. S.; Bozhko, S. I. Surface Morphology of C-Plane Sapphire (Alpha-Alumina) Produced by High Temperature Anneal. *Surf. Sci.* **2010**, *604*, 1294–1299.

40. Maruyama, B.; Ohuchi, F. S. H_2O Catalysis of Aluminum Carbide Formation in the Aluminum-Silicon Carbide System. *J. Mater. Res.* **1991**, *6*, 1131–1134.

41. Tsoukleri, G.; Parthenios, J.; Papagelis, K.; Jalil, R.; Ferrari, A. C.; Geim, A. K.; Novoselov, K. S.; Galiotis, C. Subjecting a Graphene Monolayer to Tension and Compression. *Small* **2009**, *5*, 2397–2402.

42. Das, A.; Pisana, S.; Chakraborty, B.; Piscanec, S.; Saha, S. K.; Waghmare, U. V.; Novoselov, K. S.; Krishnamurthy, H. R.; Geim, A. K.; Ferrari; et al. Monitoring Dopants by Raman Scattering in an Electrochemically Top-Gated Graphene Transistor. *Nat. Nanotechnol.* **2008**, *3*, 210–215.

43. Frank, O.; Mohr, M.; Maultzsch, J.; Thomsen, C.; Riaz, I.; Jalil, R.; Novoselov, K. S.; Tsoukleri, G.; Parthenios, J.; Papagelis, K.; et al. Raman 2D-Band Splitting in Graphene: Theory and Experiment. *ACS Nano* **2011**, *5*, 2231–2239.

44. He, R.; Zhao, L. Y.; Petrone, N.; Kim, K. S.; Roth, M.; Hone, J.; Kim, P.; Pasupathy, A.; Pinczuk, A. Large Physisorption Strain in Chemical Vapor Deposition of Graphene on Copper Substrates. *Nano Lett.* **2012**, *12*, 2408–2413.

45. Ferralis, N.; Maboudian, R.; Carraro, C. Evidence of Structural Strain in Epitaxial Graphene Layers on 6H-SiC(0001). *Phys. Rev. Lett.* **2008**, *101*, 156801-1–156801-4.

46. Blochl, P. E. Projector Augmented-Wave Method. *Phys. Rev. B* **1994**, *50*, 17953–17979.

47. Kresse, G.; Joubert, D. From Ultrasoft Pseudopotentials to the Projector Augmented-Wave Method. *Phys. Rev. B* **1999**, *59*, 1758–1775.

48. Perdew, J. P.; Burke, K.; Ernzerhof, M. Generalized Gradient Approximation Made Simple. *Phys. Rev. Lett.* **1996**, *77*, 3865–3868.

49. Perdew, J. P.; Burke, K.; Ernzerhof, M. Generalized Gradient Approximation Made Simple (vol 77, pg 3865, 1996). *Phys. Rev. Lett.* **1997**, *78*, 1396–1396.

50. Dion, M.; Rydberg, H.; Schroder, E.; Langreth, D. C.; Lundqvist, B. I. Van der Waals Density Functional for General Geometries. *Phys. Rev. Lett.* **2004**, *92*, 246401-1–246401-4.

51. Klimes, J.; Bowler, D. R.; Michaelides, A. Van der Waals Density Dunctionals Applied to Solids. *Phys. Rev. B* **2011**, *83*, 195131-1–195131-13.

52. Kresse, G.; Hafner, J. Ab Initio Molecular Dynamics for Liquid-Metals. *Phys. Rev. B* **1993**, *47*, 558–561.

53. Kresse, G.; Hafner, J. Ab Initio Molecular-Dynamics Simulation of the Liquid-Metal Amorphous-Semiconductor Transition in Germanium. *Phys. Rev. B* **1994**, *49*, 14251–14269.

54. Kresse, G.; Furthmuller, J. Efficiency of Ab-Initio Total Energy Calculations for Metals and Semiconductors using a Plane-Wave Basis Set. *Comput. Mater. Sci.* **1996**, *6*, 15–50.

55. Kresse, G.; Furthmuller, J. Efficient Iterative Schemes for Ab Initio Total-Energy Calculations Using a Plane-Wave Basis Set. *Phys. Rev. B* **1996**, *54*, 11169–11186.